ACSNANO

www.acsnano.org

ARTICLE

Highly Crystalline Poly(heptazine imide)-Based Carbonaceous Anodes for Ultralong Lifespan and Low-Temperature Sodium-Ion Batteries

Ying Wang,[#] Hongguan Li,[#] Boyin Zhai, Xinglong Li, Ping Niu, Jérémy Odent, Shulan Wang, and Li Li*

Cite This: https://doi.org/10.1021/acsnano.3c10779

Read Online

ACCESS | Metrics & More | Article Recommendations | Supporting Information

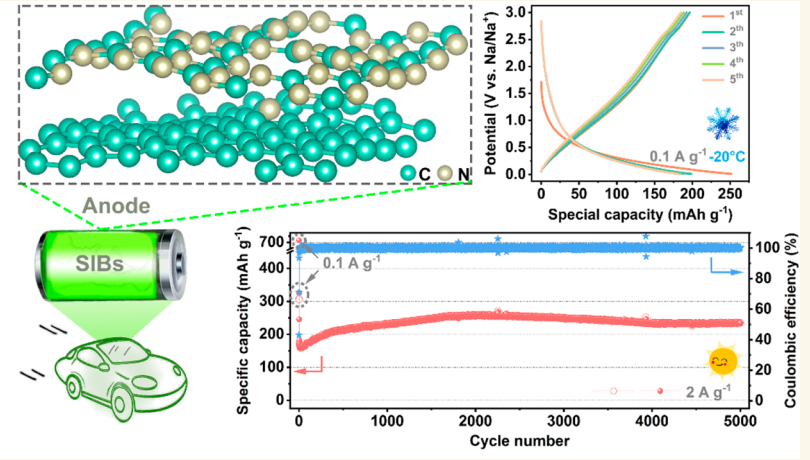

ABSTRACT: **Carbon nitrides with layered structures and scalable syntheses have emerged as potential anode choices for the commercialization of sodium-ion batteries. However, the low crystallinity of materials synthesized through traditional thermal condensation leads to insufficient conductivity and poor cycling stability, which significantly hamper their practical applications. Herein, a facile salt-covering method was proposed for the synthesis of highly ordered crystalline C_3N_4-based all-carbon nanocomposites. The sealing environment created by this strategy leads to the formation of poly(heptazine imide) (PHI), the crystalline phase of C_3N_4, with extended π-conjugation and a fully condensed nanosheet structure. Meanwhile, theoretical calculations reveal the high crystallinity of C_3N_4 significantly reduces the energy barrier for electron transition and enables the generation of efficient charge transfer channels at the heterogeneous interface between carbon and C_3N_4. Accordingly, such nanocomposites present ultrastable cycling performances over 5000 cycles, with a high reversible capacity of 245.1 mAh g^{-1} at 2 A g^{-1} delivered. More importantly, they also exhibit an outstanding low-temperature capacity of 196.6 mAh g^{-1} at −20 °C. This work offers opportunities for the energy storage use of C_3N_4 and provides some clues for developing long-life and high-capacity anodes operated under extreme conditions.**

KEYWORDS: *2D nanosheet, sodium-ion batteries, highly crystalline poly(heptazine imide), ultralong lifespan, low-temperature performances*

INTRODUCTION

The increasing demands of energy storage from portable electronics, electrical vehicles, and other applications require the development of advanced battery technologies with high energy and power densities.[1−3] The commercialized lithium-ion batteries (LIBs) have limitations due to the shortage of

Received: November 1, 2023
Revised: January 4, 2024
Accepted: January 9, 2024

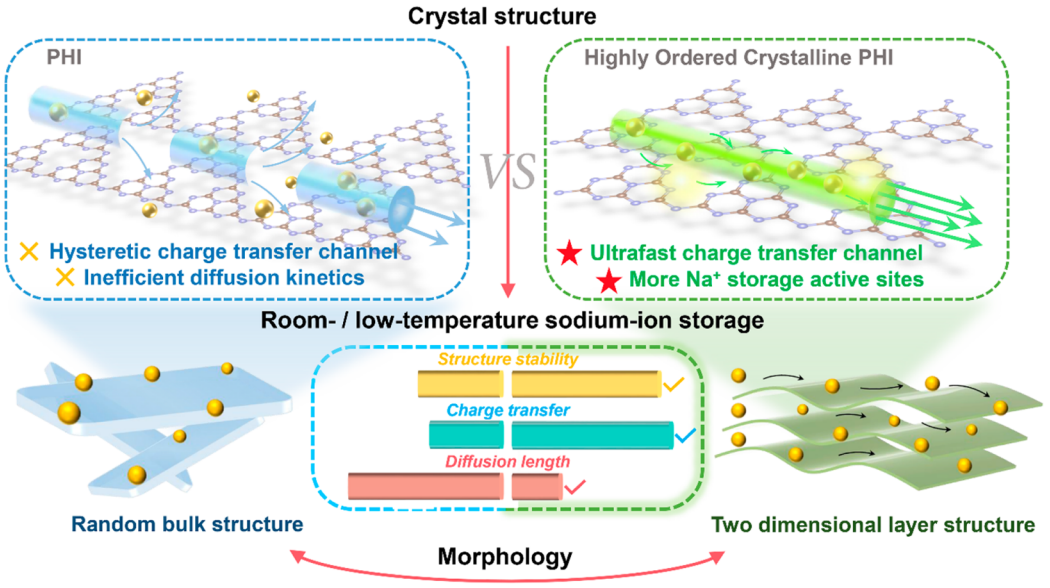

Figure 1. Design principle. Schematic of the electrochemically related structural merit differences between the conventional crystalline C_3N_4 (PHI) and the as-synthesized highly ordered crystalline PHI for SIBs.

natural reserves, and the pursuit of low-cost alternatives is in great necessity. Sodium-ion batteries (SIBs), with similar chemical properties and working mechanism to LIBs, are viewed as one of the most promising commercializable choices for large-scale energy storage.[4−6] Electrode material is the key component to determine the performances of batteries, while the larger ionic radius of Na^+ leads to the unfeasibility of conventional graphite materials used in LIBs for SIBs. However, compared with other anode choices, carbonaceous materials are still viewed as the first choice for commercialization of SIBs considering their high electronic conductivity, stable physicochemical properties under both regular and extreme conditions, and more importantly low expense.[7−11]

As a graphene analogue, graphitic carbon nitride (g-C_3N_4) has attracted increasing attention for energy use due to its unique features of a 2D-layered structure, high nitrogen content, and atomic triangular pores, though most of the current reported studies for g-C_3N_4 are focused on photocatalysis use, while its application in energy storage is still not well developed.[12−14] Its cheap and abundant source along with relatively simple processing are preferred for SIBs considering the potential economic and environmental benefits. The primary issues to prevent its extended use for SIBs are the low electrochemical conductivity and decreased crystallinity caused by irreversible reactions between metal ions and graphitic N species.[15−18] Therefore, elevating the crystallinity of g-C_3N_4 is considered as a potential avenue to improve its electrochemical performances.[19,20] Currently, the widely reported g-C_3N_4 synthesized from thermal condensation of precursors is the melon structure base with weak intralayer hydrogen bonds and substantial incompletely condensed $-NH/NH_2$ groups (always denoted as polymeric carbon nitride, PCN), which is viewed as an amorphous or semicrystalline phase.[21,22] The crystalline C_3N_4 can be synthesized under the molten salt medium, with the structure of either triazine-based (poly(triazine imide), PTI) or heptazine-based (poly(heptazine imide), PHI) subunits, depending on the processing conditions.[23−25] However, although PTI or PHI has shown improved crystallinity compared with the conventional PCN, the formation of undesired structural defects and incomplete condensation of nitrogen-containing precursors during their synthesis still restrain the elevation of structural ordering to a high level and thus deteriorate charge migration as well as Na^+ storage kinetics. Until now, despite the progress made in the production of graphene and its analogues, the development of C_3N_4-based materials with high crystallinity still remains highly challenging.

Herein, we demonstrate a simple method to synthesize highly crystalline PHI-based carbonaceous anodes for SIBs. Compared with the known crystalline C_3N_4 with PHI structure, a C_3N_4 with fully condensed nanosheet structure and elevated structural ordering can be generated through a simple salt-covering route. The further enhanced crystallinity with reduced undesired structural defects endows materials with ultrafast charge transfer channels and increased active sites for Na^+ storage, which remits the issues arising from the low crystallinity of the conventional C_3N_4 anodes (Figure 1). Meanwhile, the sealing environment provided by this strategy prevents the escape of gases and losses of intermediates and thus achieves the effective exfoliation of C_3N_4 and hierarchical pore creation, leading to the formation of a 2D nanosheet structure with high surface active sites exposed and significantly shortened diffusion lengths of ions. The nitrogen configuration is also optimized with the high content of pyridinic N species and minimized density of graphitic N, which are viewed as prerequisites for achieving high rate capability and cycling performances for C_3N_4-related batteries. Benefiting from these intrinsic features, the as-prepared material exhibited outstanding performances at both room and low temperatures (−20 °C). These results demonstrate its high potential for practical use, especially under low-temperature conditions, which is rarely reported for the electrode materials of SIBs.

RESULTS AND DISCUSSION

Morphology and Structure Analysis. Both samples CK-CNC (covered KCl-carbon nitride/carbon) and MK-CNC

https://doi.org/10.1021/acsnano.3c10779
ACS Nano XXXX, XXX, XXX−XXX

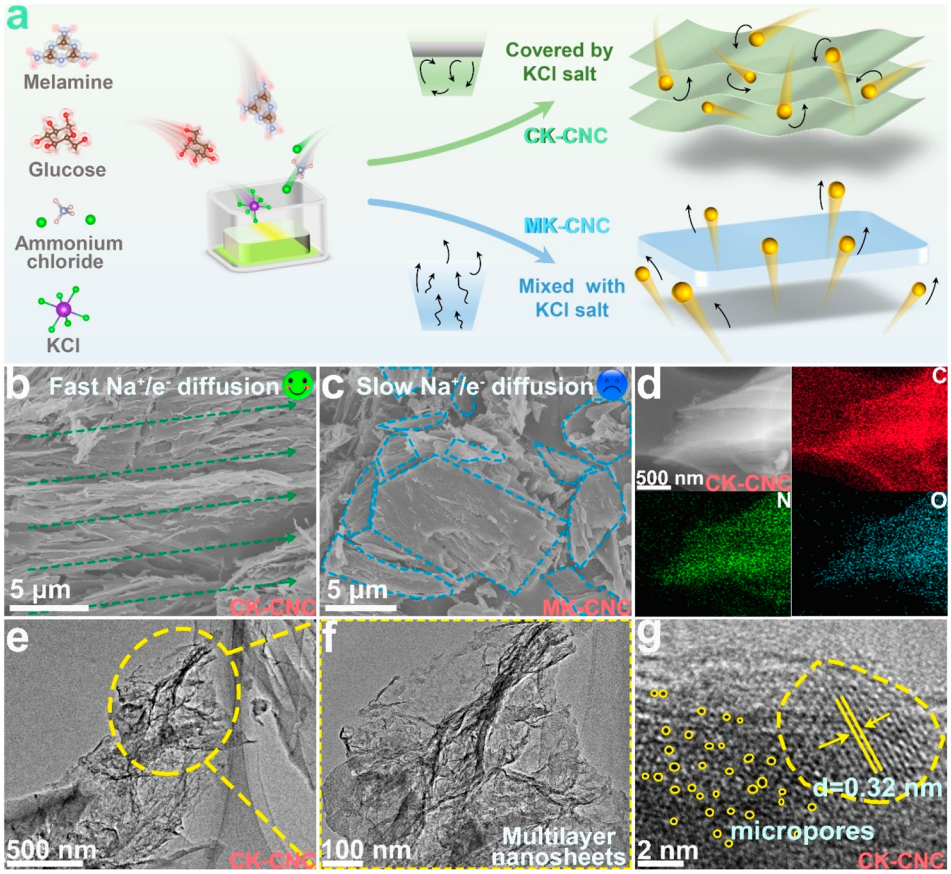

Figure 2. Morphology investigation of CK-CNC and MK-CNC. (a) Schematic illustration of the synthesis of CK-CNC and MK-CNC through KCl salted strategy. SEM images of (b) CK-CNC and (c) MK-CNC. (d) EDX elemental mappings of C, N, and O and (e,f) TEM and (g) HRTEM images of CK-CNC.

(mixed KCl-carbon nitride/carbon) are synthesized through the salted method for the polymerization of melamine, which is required for the synthesis of crystalline C_3N_4 (PHI).[23−25] The only difference in processing procedures between them is the means of KCl addition, either by fully covering or by uniform mixing (Figure 2a). Compared with the traditional mixing treatment, the salt-covering method can provide a sealing environment for the full condensation of a carbon nitride precursor and extend the in-plane π-conjugation, leading to the formation of a fully condensed structure with high crystallinity for carbon nitride. Furthermore, the salt covering can prevent the escape of endogenous NH_3, which is generated from the decomposition of ammonium chloride and serves as the pore-creating template, as well as the nitrogen-doped source. The pressure environment is also beneficial for accelerating the carbonization of glucose (the carbon source) and enhancing the electrical conductivity of the formed carbonaceous framework.[26,27] The detailed microscopic analysis (scanning electron microscopy, SEM) shows that the synthesized CK-CNC presented a layered nanosheet structure with an interconnected hierarchical porous network (Figure 2b, Figures S1 and S2), which is hardly observed for the traditional carbon nitride-based materials that always show the large bulk with little effective pore structure (Figure S3). Such a favorable layered and hierarchical porous structure can effectively relieve large volume expansion during sodiation/desodiation and facilitate electron/ion transport. Besides, the multihomogeneous-layer structure can effectively improve the mechanical strength of electrodes and prevent structural collapse during discharging/charging, which is the prerequisite for achieving the long-life performances of batteries.[28−30] The hierarchical porous structure can also provide abundant channels for ion and electron transfer and thus facilitate the charge storage kinetics. These layered 2D structures with porous network may be derived from the sealed gases (such as NH_3 and CO_2 from the decomposition of ammonium chloride and glucose, etc.) that etch and exfoliate the carbonaceous network under the internal pressure from salt covering.[31] As a comparison, MK-CNC showed a large bulk structure composed of particles in the micron size (Figure 2c and Figure S4). The energy-dispersive X-ray (EDX) elemental mapping demonstrates a uniform distribution of C, N, and O elements without hot spots (Figure 2d). High-magnification transmission electron microscopy (TEM) images (Figure 2e,f) further confirm the 2D layered sheets with abundant porous structure, which ensures rapid Na^+ diffusion and robust structure stability. A lattice spacing of 0.32 nm was obtained through high-resolution TEM (HR-TEM) analysis (Figure 2g), which is consistent with the data of the (002) plane of the poly(heptazine imide) structure, further confirming the formation of highly crystalline PHI in the CK-CNC.

The phase composition of MK-CNC and CK-CNC was characterized by X-ray diffraction (XRD) patterns, as shown in Figure 3a. The main PHI peaks that are related to the interlayer stacking of conjugated aromatic groups are buried in the wide peaks of turbostratic carbon with $\pi-\pi$ interaction,

https://doi.org/10.1021/acsnano.3c10779
ACS Nano XXXX, XXX, XXX−XXX

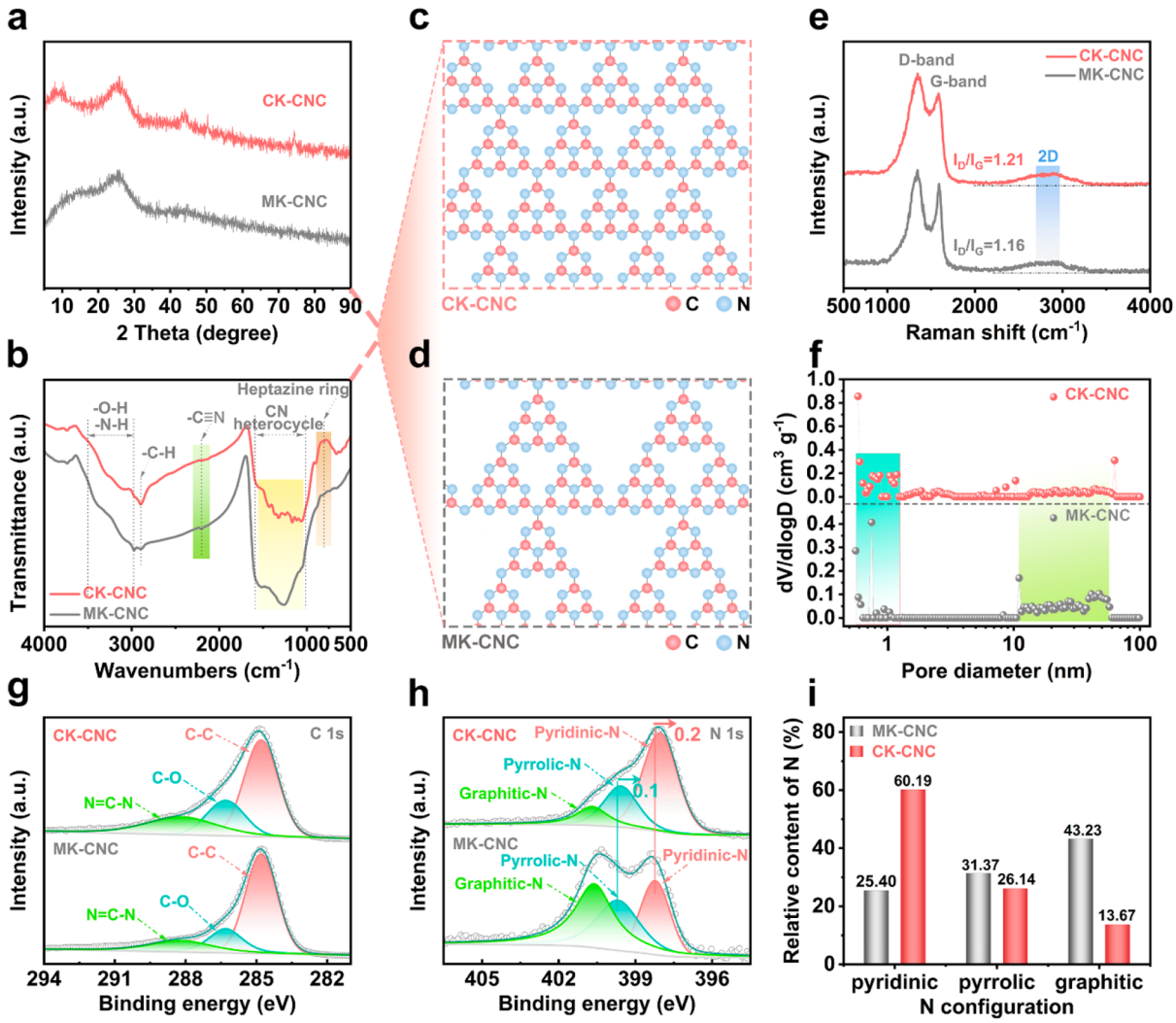

Figure 3. Structural comparison between samples. (a) XRD patterns, (b) FT-IR spectra, (c,d) PHI structures, (e) Raman spectra, and (f) pore size distribution of CK-CNC and MK-CNC. High-resolution XPS spectra of (g) C 1s and N 1s along with (i) the proportion of different N configurations within CK-CNC and MK-CNC.

which is consistent with the previous reports of carbonaceous composites.[32−34] However, the characteristic diffraction peak of PHI at 8.0° that is related to the (100) plane of crystalline C_3N_4 can still be observed in the pattern of CK-CNC, confirming the successful confirmation of PHI within the composite.[35−38] In contrast, the absence of a peak at 8.0° for MK-CNC highlights the high crystallinity and in-plane regularity of PHI in CK-CNC. Furthermore, CK-CN (covered KCl-carbon nitride) without the addition of glucose presented clear characteristic peaks of PHI (Figure S5), and its stronger and sharper peaks than those of MK-CN (mixed KCl-carbon nitride) further verify the highly structural ordering of samples synthesized from the salt-covering method. Fourier transform infrared spectra (FT-IR) were employed to further validate the structure and chemical features of samples, as shown in Figure 3b. The characteristic peaks of both samples are mainly related to the heptazine-based structure, indicating the identical framework of CK-CNC and MK-CNC. The peak at 806 cm^{-1} represents the out-of-plane bending mode of the heptazine ring, while the fingerprint peak at 1000−1700 cm^{-1} is assigned to the stretching vibration mode of the conjugated C−N ring.[39−41] The stronger intensities of these two peaks within the spectrum of CK-CNC than those of MK-CNC demonstrate the fully condensed structure of PHI within CK-CNC. Correspondingly, the stronger signal of cyano groups (−C≡N) at 2206 cm^{-1} also indicates the maintenance of large numbers of cyano-terminal groups within MK-CNC, leading to the low condensed structure with limited crystallinity.[42,43] Both aforementioned XRD and FT-IR results confirm the formation of a highly crystalline PHI phase within CK-CNC, and the detailed structures of the samples were presented in Figure 3c,d.

Raman spectra were then recorded to further investigate the detailed chemical configurations of the samples (Figure 3e). No clear characteristic peak for C_3N_4 was observed, which is consistent with the previous reports.[38,44−46] The two typical peaks at 1344 and 1590 cm^{-1} correspond to the disordered carbon (D-band) and graphitic carbon (G-band), respectively, confirming the presence of carbon in MK-CNC and CK-CNC.[47] Compared with MK-CNC, CK-CNC exhibited low peak intensity due to the favorable interfacial charge transfer between carbon and PHI.[44,48] Besides, the slightly higher I_D/I_G value of CK-CNC (1.21) than that of MK-CNC (1.16) indicates the more localized defects in the carbon matrix of

https://doi.org/10.1021/acsnano.3c10779
ACS Nano XXXX, XXX, XXX−XXX

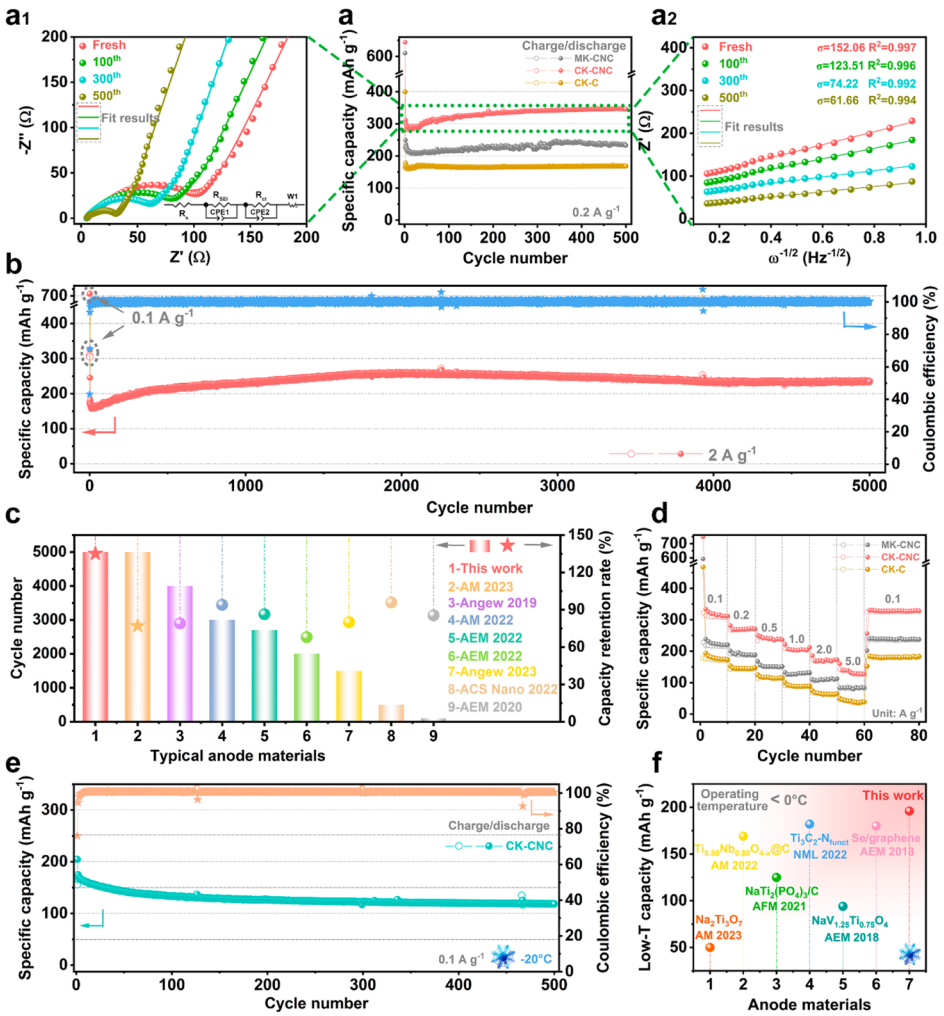

Figure 4. Electrochemical performances of samples in half-cell configurations. (a) Cycling performances of MK-CNC, CK-CNC, and CK-C at 0.2 A g^{-1}. (a_1) Nyquist plots (with equivalent circuit simulated in the inset) of CK-CNC fresh and cycled electrodes at 0.2 A g^{-1} for 100−500 cycles and (a_2) the corresponding fitting of Warburg impedance coefficients (σ). (b) Long-term cycling performances of CK-CNC at 2 A g^{-1} with a preactivation at 0.1 A g^{-1} for the initial two cycles. (c) Electrochemical performance comparison of this work with reported typical anode materials for SIBs. (d) Rate capabilities of samples from 0.1 to 5 A g^{-1}. (e) Cycling stability of the CK-CNC tested at −20 °C. (f) Low-temperature performance comparison of CK-CNC with other reported anodes for SIBs.

CK-CNC composites,[49] which is beneficial for providing more sufficient electrochemical active sites and promoting the pseudocapacitive kinetic behaviors.[50−52] CK-CNC also presented a high surface area of 158.65 m^2 g^{-1}, which is predictably higher than that of the MK-CNC composite (61.12 m^2 g^{-1}) (Figure 3f and Figure S6). Its highly porous structure with a large pore volume (Table S1) is also consistent with SEM and TEM results. The Brunauer−Emmet−Teller (BET) results confirm that the CK-CNC composite possesses higher surface area and abundant mesoporous structure to provide sufficient active sites and enhance the charge transfer kinetics.

To elucidate the bonding information and surface states of samples, X-ray photoelectron spectroscopy (XPS) measurements were performed, and the survey spectra confirm the existence of C, N, and O elements without other impurities (Figures S7 and S8). The apparently higher concentration of the N element in CK-CNC (24.33 at. %) than that of MK-CNC (8.57 at. %) indicates that the salt-covering method achieved full condensation and conversion of the N-containing precursor (Table S2). The high-resolution C 1s spectra (Figure 3g) presented three peaks at 284.8, 286.3, and 288.2 eV, corresponding to C−C, C−O, and N=C−N, respectively.[34,44,53] It is worth noting that, compared to MK-CNC, CK-CNC presented a relatively high content of N=C−N with sp^2-bonded aromatic structure, proving the higher density of the heptazine structure for CK-CNC (Table S3).[37,54] The high-resolution N 1s spectra (Figure 3h) were deconvoluted into pyridinic-N, pyrrolic-N, and graphitic N located at 398.2/398.0 eV, 399.7/399.6 eV, and 400.6/400.6 eV, respectively.[55−57] The detailed percentages of N configurations are given in Figure 3i and Table S3. The contents of pyridinic N and pyrrolic N, which are favorable for enhancing the electrical conductivity and reduction of irreversible reactions,[17,58] are much higher in CK-CNC (86.33%) than that in MK-CNC (56.77%). The high proportion of pyridine-N and pyrrole-N guarantees abundant electroactive sites, leading to fast electrochemical kinetics and a high reversible capacity. Correspondingly, the low concentration of graphitic N (13.67%) is also beneficial for maintaining high crystallinity of C_3N_4 and enhancing Na adsorption.[59] The slight shift of

https://doi.org/10.1021/acsnano.3c10779
ACS Nano XXXX, XXX, XXX−XXX

pyridinic N and pyrrolic N peaks of CK-CNC to the lower binding energy compared with those of MK-CNC also proves the extended conjugation of PHI.[60]

Sodium Storage Performances at Different Temperatures. The electrochemical performances of as-prepared materials were first evaluated by using the anodes for the half-cell assembly. The cyclic voltammetry (CV) curve of CK-CNC for the first cycle (Figure S9) presented an irreversible peak at about 0.1 V caused by the formation of a solid electrolyte interface (SEI) layer,[8] which then disappeared after the stabilization in the following cycles. The nearly overlapping of curves for the subsequent cycles confirms the highly reversible electrochemical kinetics within the CK-CNC anode. The detailed cycling performance of CK-CNC and its controls at 0.2 A g^{-1} are shown in Figure 4a. It can be clearly observed that the reversible capacity of CK-CNC can still be maintained at 346.1 mAh g^{-1} after 500 cycles, with a capacity retention rate of up to 123.5%, which is rarely reported for the carbonaceous-based anodes of SIBs. The sodium storage properties are further investigated with galvanostatic charge−discharge (GCD) curves tested at 0.2 A g^{-1} (Figure S10). The initial discharge and charge capacities of CK-CNC and MK-CNC are 643.3/609.8 and 280.2/225.9 mAh g^{-1}, with initial Coulombic efficiency (ICE) values of 43.56% and 37.05%, respectively. The initial irreversible capacity loss is assigned to the electrolyte decomposition and irreversible formation of SEI. After the initial cycles, the Coulombic efficiency values are stabilized and close to 100%. Besides, its GCD profiles also showed a reverse capacity growth trend, which is consistent with the presented cycling performance. Correspondingly, MK-CNC and the control CK-C (covered KCl-carbon) only delivered the capacities of 232.8 and 168.5 mAh g^{-1}, which is much inferior to CK-CNC. The electrochemical impedance spectra (EIS) analysis demonstrates the much smaller charge-transfer resistance (R_{ct}) of CK-CNC than that of MK-CNC (Figure S11 and Table S4), confirming its rapid charge transfer kinetics due to the high crystallinity and extended π-conjugation structure. A further detailed investigation for the change of R_{ct} was performed with Nyquist plots collected for CK-CNC electrodes at the 0, 100th, 300th, and 500th cycles (Figure 4a$_1$), respectively. The decreased R_{ct} values from 152.06 (0) to 123.5 (100th), 74.22 (300th), and 61.66 Ω (500th) along with the increased Na^+ diffusion coefficients (D_{Na^+}) confirm the gradually reduced interface impedance and the rising Na^+ diffusion kinetics through cycling (Figure 4a$_2$ and Table S5), which lead to the reverse capacity growth of the CK-CNC electrode as shown above. The gradually stabilized SEI layer with reduced side reactions facilitates charge transfer and Na^+ diffusion, and thus the active materials are favorably accessible for activation, thereby improving the capacity through cycling.[61] On the other hand, this reverse capacity growth can only be enabled when the structural stability of active materials is sufficiently high. It also presented extraordinary cycling performance at the high current density of 2 A g^{-1} with a high capacity of 245.1 mAh g^{-1} and a retention rate of 135.1% maintained even after 5000 cycles (Figure 4b), demonstrating its excellent long-cycling life and potential practical feasibility over the commercial SIB anodes. Its performances have surpassed most of those of the earlier reported materials for SIBs and are among the highest values in all carbonaceous anodes (Figure 4c and Table S6). The Coulombic efficiency (CE) was maintained to be nearly 100% during discharging/charging. The CK-CNC anode also showed outstanding rate capabilities with the reversible capacities of 307.0, 268.9, 235.9, 211.9, 170.7, and 126.9 delivered at 0.1, 0.2, 0.5, 1.0, 2.0, and 5 A g^{-1}, respectively (Figure 4d). When the current density rebounded back to 0.1 A g^{-1}, the capacity even increased to 326.5 mAh g^{-1}, implying its high structural durability and superior reaction kinetics. In contrast, MK-CNC and CK-C showed inferior rate performances with the values of 216.1/170.3, 187.2/146.4, 150.4/114.1, 130.5/88, 111.9/64.4, and 80.8/38.9 mAh g^{-1} at 0.1, 0.2, 0.5, 1.0, 2.0, and 5 A g^{-1}, respectively.

To further probe the Na^+ storage kinetics of CK-CNC and MK-CNC, the capacitive-controlled and diffusion-controlled charge contributions were estimated with CV curves systematically recorded at different scan rates of 0.1−1.0 mV s^{-1} (Figures S12a−S13a). The well-maintained shape of curves with the increase in scanning rate demonstrates their good electrode reactivity with reversible electrochemical reactions. The corresponding calculated *b*-values of CK-CNC and MK-CNC electrodes were 0.78/0.77 and 0.89/0.92 (Figures S12b−S13b), indicating the capacitive-controlled mechanism dominates in both samples for charge storage. More precisely, the higher capacitive contribution of CK-CNC than that of MK-CNC (Figures S14 and S15) proves its more rapid sodiation/desodiation process for fast charge transfer, which ensures the superior electrochemical activity and ultralong cycling life of CK-CNC. The electrical conductivity of samples was also tested (Figure S16), and CK-CNC shows higher conductivity than that of MK-CNC as expected, demonstrating its great charge transfer capability.

The structural evolution of the MK-CNC and CK-CNC electrodes before and after cycling at 2 A g^{-1} was studied in detail to investigate the structural integrity and volume change that was considered as the key factor for preventing capacity decay during discharging/charging (Figure S17). Compared with the top-view SEM images of MK-CNC that showed severe structural damage with visible fractures and cracks on the electrode surface after 5000 cycles (Figure S17a−c), CK-CNC presented the smoother surface without apparent cracking, and the 2D multilayer nanosheet stacking structure was still well-maintained (Figure S17d−f), suggesting the robust structural stability of the CK-CNC electrode. The highly ordered structure and high proportion of active pyridinic N are beneficial for relieving the internal stress produced through discharging/charging and thus achieved stabilized cycling for efficient Na^+ storage. The excellent structural integrity, negligible volume change, and rapid Na^+ transport kinetics provide the foundation for achieving inverse capacity growth in the CK-CNC electrode. The structure of CK-CNC also did not have an apparent change after cycling (Figure S18). The XPS and HRTEM analyses of CK-CNC after cycling were then performed to investigate the surface chemistry and morphology of cycled electrodes with SEI formation (Figures S19 and S20). The SEI layer provides effective protection for the CK-CNC electrode and supports its long-term cycling stability in ester-based electrolytes.[62−64]

The low-temperature electrochemical performances of the CK-CNC electrode were further analyzed to explore its potential for practical applications under stringent conditions. The different electrolyte for checking its low-temperature performances was selected (Figures S21 and S22). Its GCD curves for the initial 5 cycles presented similar sloping profiles at −20 °C, indicating its high electrode activity and structural stability (Figure S23). The CK-CNC anode delivered a high

https://doi.org/10.1021/acsnano.3c10779
ACS Nano XXXX, XXX, XXX−XXX

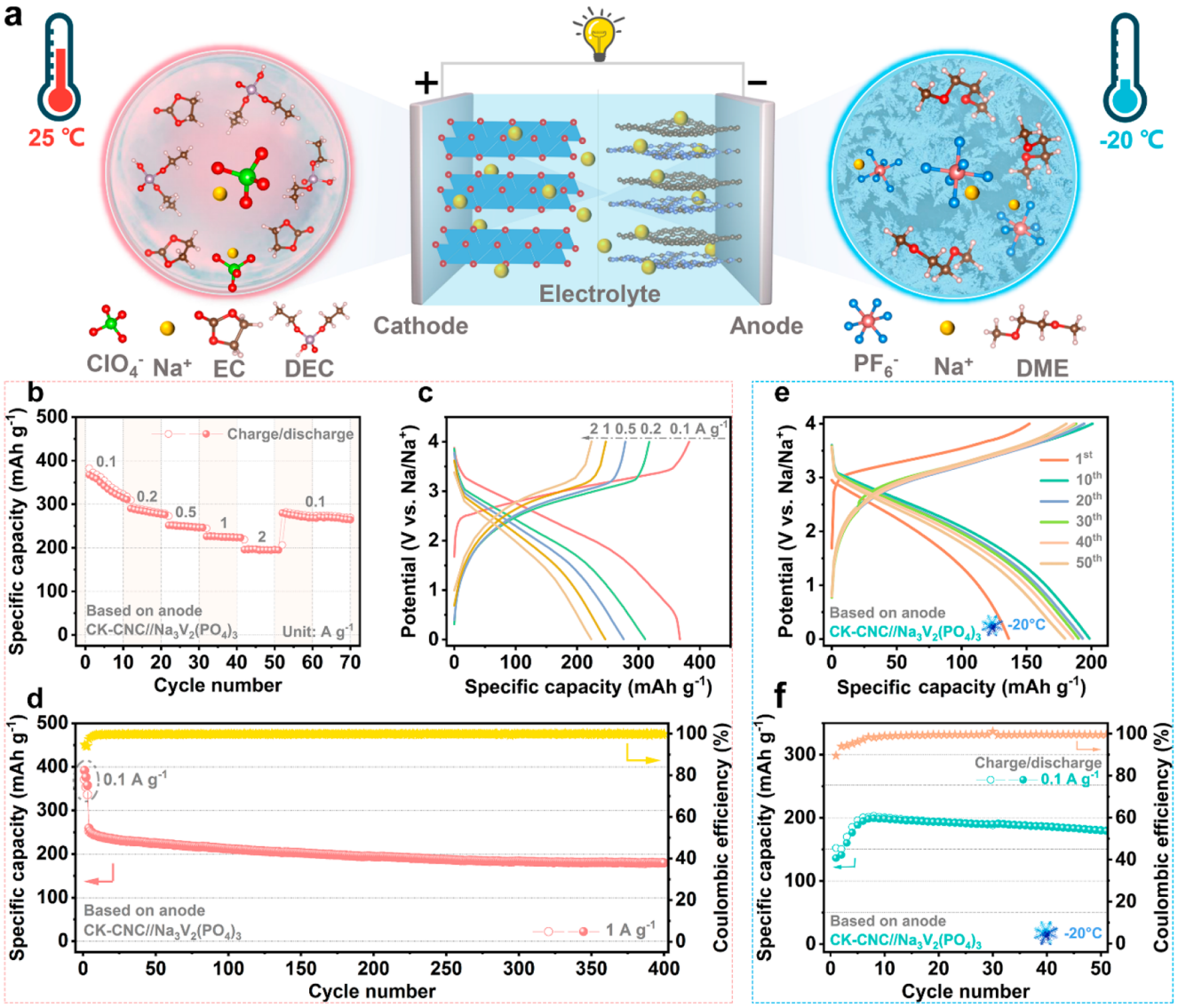

Figure 5. Electrochemical performances of the full cell tested at room temperature (25 °C) and low temperature (−20 °C). (a) Illustration of the CK-CNC//$Na_3V_2(PO_4)_3$ full cell. (b) Rate capability, (c) GCD curves, and (d) cycling performance at 1 A g^{-1} of the full cell tested at room temperature. (e) GCD curves and (f) cycling stability of the full cell tested at −20 °C.

reversible capacity of 196.6 mAh g^{-1} at 0.1 A g^{-1} with a high ICE of 78.1% that is superior to most of the reported low-temperature carbonaceous electrodes (Figure S24), demonstrating the rapid Na^+ adsorption/diffusion kinetics even at −20 °C. The CK-CNC-based electrode can still present excellent cycling performance with a reversible capacity of 118.9 mAh g^{-1} after 500 stable cycles at 0.1 A g^{-1} and a capacity retention of 76.4% (Figure 4e). Its low-temperature performances have surpassed most of the previously reported high-performance anodes that can be used under a frozen point (Figure 4f and Table S7). Strikingly, it can even show a high capacity retention of 84.1% for 6000 cycles at a high current density of 2 A g^{-1} (Figure S25). Its impressive low-temperature electrochemical performances endow the as-synthesized CK-CNC with high potential for the practical use of efficient sodium storage, especially under extreme conditions.

The full cell was then assembled by using commercial grade $Na_3V_2(PO_4)_3$ as the cathode to couple with the CK-CNC anode for performance evaluation (Figure 5a). The electrolytes used for room-temperature and frozen testing were 1.0 M $NaClO_4$ in ethylene carbonate/diethyl carbonate (EC/DEC, 1:1, v/v) with 5% fluoroethylene carbonate (FEC) and 1.0 M $NaPF_6$ in dimethyl ether (DME), respectively. As presented in Figure 5b, the CK-CNC//$Na_3V_2(PO_4)_3$ full cell delivered room-temperature reversible capacities of 314.2, 277, 246, 223.3, and 195.3 mAh g^{-1} at 0.1, 0.2, 0.5, 1, and 2 A g^{-1}, respectively, indicating its high-rate capability and fast charge storage ability. The corresponding GCD curves can maintain the original shape without a change even when the current density increased to 2 A g^{-1} (Figure 5c), which demonstrates the highly reversible reaction for charge storage in the CK-CNC-based batteries. In addition, CK-CNC//$Na_3V_2(PO_4)_3$ also showed an outstanding cycling performance with a high reversible capacity of 179.8 mAh g^{-1} delivered after 400 cycles at 1 A g^{-1}. The capacity retention maintains 71.24% with a capacity decay of only 0.0719% per cycle (Figure 5d), which is much better than the commercial benchmark.[65,66] Further-

https://doi.org/10.1021/acsnano.3c10779
ACS Nano XXXX, XXX, XXX−XXX

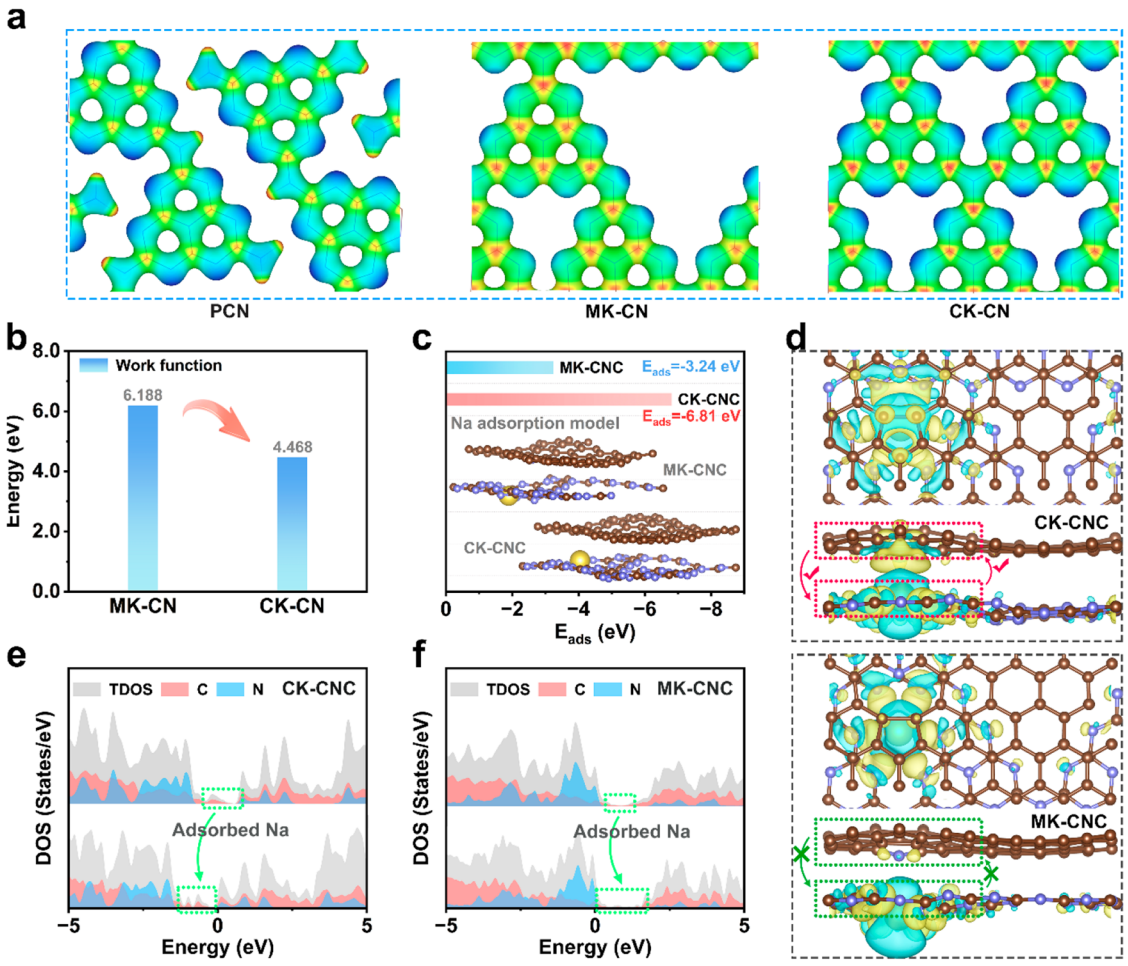

Figure 6. DFT calculations. (a) Electrostatic potential analysis of carbon nitrides with different structures. Blue and red regions represent negative and positive charges, respectively. (b) Work function calculations of carbon nitrides. (c) Adsorption energies of Na on CK-CNC and MK-CNC. (d) Charge density differences of Na adsorption in CK-CNC and MK-CNC. The yellow and cyan regions refer to charge accumulation and depletion, respectively. The total and partial density of states (TDOS and PDOS) of (e) CK-CNC and (f) MK-CNC before and after Na adsorption.

more, the full cell also showed superior low-temperature electrochemical performances tested at −20 °C. The GCD profiles of the full cell presented a high average voltage platform at 2.8 V (Figure 5e), which is crucial for devices to output high energy density. It can still display the high reversible capacity of 179.2 mAh g^{-1} after cycling at 0.1 A g^{-1}, which exceeds many previously reported excellent full-cell assemblies that present a low-temperature sodium storage capability (Figure 5f and Table S8).

Theoretical Analysis. DFT calculations were then performed to investigate the in-depth influence of the crystalline structure on the electronic properties and Na^+ storage behaviors of the composites. Herein, MK-CN with PHI structure and CK-CN with the fully extended conjugated system and highly ordered structure, as confirmed by the previously presented structural characterizations, were modeled, while the traditional polymeric carbon nitride (PCN) with the Melon structure that is reported most in the previous literature was also listed as a reference.[54,67] The optimized structural models and the corresponding electron density difference are shown in Figures S26−S28. After the adsorption of Na (Figures S29−S31), it can be clearly observed from the charge density difference map that significant charge transfer occurs between Na^+ and CK-CN. Furthermore, the corresponding electrostatic potential analysis (Figure 6a) implies the occurrence of the most favorable Na^+ adsorption within CK-CN among three structures with the low-strength potential.[68] The hexagonal pore inside of the heptazine unit distributed negative charge centers, in which there existed suitable Na^+ accommodation sites. Higher density in-plane heptazine units in the CK-CNC can accelerate the Na^+ diffusion and provide more sodium storage capacities. In addition, the work function calculation was performed to compare the internal driving force of electron transfer, and CK-CN showed the lower value (4.468 eV) than MK-CN (6.188 eV) (Figure 6b), indicating its smaller energy barrier for electron transitions and faster charge transfer kinetics.[69,70] The highly ordered crystalline structure of CK-CN with low concentration of undesired structural defects is favorable for promoting electron migration and enhancing Na adsorption capability, thus endowing the electrode with excellent rate performance.[70,71]

Carbon was then introduced into the models (Figure S32), and the corresponding Na adsorption energies were calculated (Figure 6c). Compared with MK-CNC (−3.24 eV), CK-CNC exhibited a lower adsorption energy (−6.81 eV), indicating its

https://doi.org/10.1021/acsnano.3c10779
ACS Nano XXXX, XXX, XXX−XXX

stronger Na-ion capture capability that is consistent with the result shown in CK-CN. The charge density difference analysis of CK-CNC clearly shows charge transfer channels at the heterogeneous interface between CK-CN and the carbon layer (Figure 6d), which can effectively accelerate ion/electron transport between components and thereby ensure fast reaction kinetics with a low Na^+ diffusion barrier. This interaction enhances the possibility of CK-CNC for accommodating more sodium, further ensuring the excellent Na^+ storage ability of CK-CNC at a low temperature. As a comparison, no apparent electronic structural transition is found at the heterojunction interface within MK-CNC. To further characterize the differences of their electronic properties, the density of states (DOS) was calculated for MK-CNC and CK-CNC to explore the structural changes before and after Na adsorption (Figure 6e,f). Compared with MK-CNC, CK-CNC showed 2p continuous orbital electron filling at the Fermi level, indicating significant enhancement of electronic conductivity for facilitating Na adsorption. The aforementioned calculation result confirms the CK-CNC with highly ordered structure can ensure high Na^+ adsorption capability and enhanced electrical conductivity from components along with electrochemically favorable heterostructure interfaces for rapid charge transfer, which accounts for its outstanding long-term cycling stability and low-temperature capacity performances.

CONCLUSIONS

In summary, a carbonaceous nanocomposite with highly ordered crystalline PHI was prepared by an unusual KCl salt-recovering method. Compared with the traditional PCN with amorphous heptazine-based melon and known crystalline PHI with undesired structural defects, the as-prepared C_3N_4 presented a fully condensed structure and extended π-conjugation, significantly elevating its structural ordering and achieving high crystallinity. After coupling with carbon, the corresponding nanocomposite also exhibited multiple electrochemically favorable features, including a 2D layered nanosheet structure and a high proportion of active N species. DFT analysis reveals that the electrical conductivity of material is greatly enhanced with continuous orbital electron filling at the Fermi level, while the reduced energy barrier for electron transitions along with easy Na^+ adsorption and high driving force for charge transfer are achieved. As the SIB anode, the synthesized material delivered a high reversible capacity of 245.1 mAh g^{-1} at 2 A g^{-1} over extended 5000 cycles with a high-capacity retention rate of 135.1%. More importantly, it also delivered a high reversible capacity of 196.6 mAh g^{-1} at −20 °C, and the assembled CK-CNC//$Na_3V_2(PO_4)_3$ full cell can present a high reversible capacity of 179.2 mAh g^{-1} at 0.1 A g^{-1} after cycling (−20 °C). This work extends the energy use of carbon nitrides and enriches the nanomaterial library of anode materials for SIBs operated at low temperatures.

METHODS

Sample Preparation. Melamine, glucose, and ammonium chloride were uniformly mixed by fine grinding in a mass ratio of 1:1:1. Afterward, the mixture was transferred to a crucible and carefully covered with KCl salt, followed by annealing at 300 °C for 1 h, 550 °C for 2 h, and 600 °C for 2 h in a tube furnace under N_2. After cooling to room temperature, the overlying KCl salt layer could be directly removed, and the obtained sample was labeled as CK-CNC (covered KCl-carbon nitride/carbon). For comparison, the mixture was ground and mixed evenly with KCl salt following the same treatment. The sample obtained after full salt removal was designated as MK-CNC (mixed KCl-carbon nitride/carbon). The control sample without the addition of mealmine in the synthesis procedure of CK-CNC was designated as CK-C (covered KCl-carbon). Correspondingly, the samples without the addition of glucose in the synthesis procedure of CK-CNC and MK-CNC were designated as CK-CN (covered KCl-carbon nitride) and MK-CN (mixed KCl-carbon nitride), respectively.

Material Characterizations. The morphological features of samples were recorded by employing scanning electron microscopy (SEM, JSM-6700F). Transmission electron microscopy (TEM) and high-resolution transmission electron microscopy (HRTEM) with energy-dispersive X-ray (EDX) spectroscopy analysis were conducted by using a spherical aberration-corrected transmission electron microscope (AC-TEM, JEOL, JEM-ARM200F) to investigate thoroughly the microstructure and morphology of samples. The phase composition and spectroscopic characteristics were determined with an X-ray diffractometer (XRD, Shimadzu, XRD-7000) via Cu Kα radiation, Fourier-transform infrared spectra (FT-IR, Bruker VERTEX70), and Raman spectroscopy (Horiba LabRAM HR Evolution, 633 nm). The chemical structure and surface properties were checked using X-ray photoelectron spectroscopy (XPS, Thermo Scientific K-Alpha) with Al Kα radiation. The specific surface area and pore size distribution were collected by a N_2 adsorption/desorption instrument (Quantachrome Autosorb IQ). The electrical conductivity was measured by a four-probe method (Keithley, 2450 SourceMeter). Other details about chemicals and electrochemical characterizations can be found in the Supporting Information.

ASSOCIATED CONTENT

Supporting Information

The Supporting Information is available free of charge at https://pubs.acs.org/doi/10.1021/acsnano.3c10779.

Experimental details; XRD pattern, SEM, TEM, XPS spectra, Raman spectrum, N_2 adsorption−desorption isotherms, pore size distribution curve; electrochemical data; comparison of electrochemical performance; CV profiles (pseudocapacitive contributions, *b* value); EIS curves (Na^+ diffusion coefficient); ex situ SEM; DFT results (PDF)

AUTHOR INFORMATION

Corresponding Author

Li Li − *School of Metallurgy, Northeastern University, Shenyang 110819, P. R. China; State Key Laboratory of Rolling and Automation, Northeastern University, Shenyang 110819 Liaoning, P. R. China; Foshan Graduate School of Innovation, Northeastern University, Foshan 528311 Guangdong, P. R. China;* orcid.org/0000-0003-2308-916X; Email: lilicmu@alumni.cmu.edu

Authors

Ying Wang − *School of Metallurgy, Northeastern University, Shenyang 110819, P. R. China; State Key Laboratory of Rolling and Automation, Northeastern University, Shenyang 110819 Liaoning, P. R. China; Foshan Graduate School of Innovation, Northeastern University, Foshan 528311 Guangdong, P. R. China*

Hongguan Li − *School of Metallurgy, Northeastern University, Shenyang 110819, P. R. China; State Key Laboratory of Rolling and Automation, Northeastern University, Shenyang 110819 Liaoning, P. R. China; Foshan Graduate School of Innovation, Northeastern University, Foshan 528311 Guangdong, P. R. China*

https://doi.org/10.1021/acsnano.3c10779
ACS Nano XXXX, XXX, XXX−XXX

Boyin Zhai − *Department of Chemistry, College of Science, Northeastern University, Shenyang 110819 Liaoning, P. R. China*

Xinglong Li − *Department of Chemistry, College of Science, Northeastern University, Shenyang 110819 Liaoning, P. R. China*

Ping Niu − *School of Metallurgy, Northeastern University, Shenyang 110819, P. R. China; State Key Laboratory of Rolling and Automation, Northeastern University, Shenyang 110819 Liaoning, P. R. China; Foshan Graduate School of Innovation, Northeastern University, Foshan 528311 Guangdong, P. R. China;* orcid.org/0000-0002-4781-3098

Jérémy Odent − *Laboratory of Polymeric and Composite Materials (LPCM), Center of Innovation and Research in Materials and Polymers (CIRMAP), University of Mons (UMONS), 7000 Mons, Belgium;* orcid.org/0000-0002-3038-846X

Shulan Wang − *Department of Chemistry, College of Science, Northeastern University, Shenyang 110819 Liaoning, P. R. China*

Complete contact information is available at: https://pubs.acs.org/10.1021/acsnano.3c10779

Author Contributions

#Y. W. and H. L. contributed equally to this work.

Notes

The authors declare no competing financial interest.

ACKNOWLEDGMENTS

This work was supported by the National Natural Science Foundation of China (22378055), Applied Basic Research Program of Liaoning (2022JH2/101300200), Guangdong Basic and Applied Basic Research Foundation (2022A1515140188), Fundamental Research Funds for the Central Universities (N2002005, N2125004, N2225044, and N232410019). We also appreciate the instrumental analysis from Analytical and Testing Center, Northeastern University.

REFERENCES

(1) Meng, W.; Dang, Z.; Li, D.; Jiang, L. Long-cycle-life sodium-ion battery fabrication via a unique chemical bonding interface mechanism. *Adv. Mater.* **2023**, *35*, 2301376.

(2) Liu, H.; Cai, X.; Zhi, X.; Di, S.; Zhai, B.; Li, H.; Wang, S.; Li, L. An amorphous anode for proton battery. *Nano-Micro Lett.* **2023**, *15*, 24.

(3) Zhou, X.; Zhang, Q.; Zhu, Z.; Cai, Y.; Li, H.; Li, F. Anion-reinforced solvation for a gradient inorganic-rich interphase enables high-rate and stable sodium batteries. *Angew. Chem., Int. Ed.* **2022**, *61*, e202205045.

(4) Wang, Y.; Li, H.; Chen, S.; Zhai, B.; Di, S.; Gao, G.; Lee, S.; Chun, S.; Wang, S.; Li, L. An ultralong-life SnS-based anode through phosphate-induced structural regulation for high-performance sodium ion batteries. *Science Bulletin* **2022**, *67*, 2085−2095.

(5) Di, S.; Li, H.; Zhai, B.; Zhi, X.; Niu, P.; Wang, S.; Li, L. A crystalline carbon nitride-based separator for high-performance lithium metal batteries. *Proc. Natl. Acad. Sci. U. S. A.* **2023**, *120*, e2302375120.

(6) Ren, M.; Zhao, S.; Gao, S.; Zhang, T.; Hou, M.; Zhang, W.; Feng, K.; Zhong, J.; Hua, W.; Indris, S.; Zhang, K.; Chen, J.; Li, F. Homeostatic solid solution in layered transition-metal oxide cathodes of sodium-ion batteries. *J. Am. Chem. Soc.* **2023**, *145*, 224−233.

(7) Yin, B.; Liang, S.; Yu, D.; Cheng, B.; Egun, I. L.; Lin, J.; Xie, X.; Shao, H.; He, H.; Pan, A. Increasing accessible subsurface to improving rate capability and cycling stability of sodium-ion batteries. *Adv. Mater.* **2021**, *33*, 2100808.

(8) Li, H.; Di, S.; Niu, P.; Wang, S.; Wang, J.; Li, L. A durable half-metallic diatomic catalyst for efficient oxygen reduction. *Energy Environ. Sci.* **2022**, *15*, 1601−1610.

(9) Zhang, C.; Liu, X.; Li, Z.; Zhang, C.; Chen, Z.; Pan, D.; Wu, M. Nitrogen-doped accordion-like soft carbon anodes with exposed hierarchical pores for advanced potassium-ion hybrid capacitors. *Adv. Funct. Mater.* **2021**, *31*, 2101470.

(10) Dou, X.; Hasa, I.; Saurel, D.; Vaalma, C.; Wu, L.; Buchholz, D.; Bresser, D.; Komaba, S.; Passerini, S. Hard carbons for sodium-ion batteries: Structure, analysis, sustainability, and electrochemistry. *Mater. Today* **2019**, *23*, 87−104.

(11) Fang, H.; Gao, S.; Ren, M.; Huang, Y.; Cheng, F.; Chen, J.; Li, F. Dual-function presodiation with sodium diphenyl ketone towards ultra-stable hard carbon anodes for sodium-ion batteries. *Angew. Chem., Int. Ed.* **2023**, *62*, e202214717.

(12) Wang, Y.; Liu, L.; Ma, T.; Zhang, Y.; Huang, H. 2D graphitic carbon nitride for energy conversion and storage. *Adv. Funct. Mater.* **2021**, *31*, 2102540.

(13) Besharat, F.; Ahmadpoor, F.; Nezafat, Z.; Nasrollahzadeh, M.; Manwar, N. R.; Fornasiero, P.; Gawande, M. B. Advances in carbon nitride-based materials and their electrocatalytic applications. *ACS Catal.* **2022**, *12*, 5605−5660.

(14) Lu, C.; Chen, X. Nanostructure engineering of graphitic carbon nitride for electrochemical applications. *ACS Nano* **2021**, *15*, 18777−18793.

(15) Zhao, D.; Zhang, Z.; Ren, J.; Xu, Y.; Xu, X.; Zhou, J.; Gao, F.; Tang, H.; Liu, S.; Wang, Z.; Wang, D.; Wu, Y.; Liu, X.; Zhang, Y. Fe_2VO_4 nanoparticles on rGO as anode material for high-rate and durable lithium and sodium ion batteries. *Chem. Eng. J.* **2023**, *451*, 138882.

(16) Kim, J. W.; Augustyn, V.; Dunn, B. The effect of crystallinity on the rapid pseudocapacitive response of Nb_2O_5. *Adv. Energy Mater.* **2012**, *2*, 141−148.

(17) Yuan, Y.; Chen, Z.; Yu, H.; Zhang, X.; Liu, T.; Xia, M.; Zheng, R.; Shui, M.; Shu, J. Heteroatom-doped carbon-based materials for lithium and sodium ion batteries. *Energy Storage Mater.* **2020**, *32*, 65−90.

(18) Chen, W.; Wan, M.; Liu, Q.; Xiong, X.; Yu, F.; Huang, Y. Heteroatom-doped carbon materials: Synthesis, mechanism, and application for sodium-ion batteries. *Small Methods* **2019**, *3*, 1800323.

(19) Wang, Z.; Jin, B.; Peng, J.; Su, W.; Zhang, K.; Hu, X.; Wang, G.; Park, J. H. Engineered polymeric carbon nitride additive for energy storage materials: A review. *Adv. Funct. Mater.* **2021**, *31*, 2102300.

(20) Huo, T.; Deng, Q.; Yu, F.; Wang, G.; Xia, Y.; Li, H.; Hou, W. Ion-induced synthesis of crystalline carbon nitride ultrathin nanosheets from mesoporous melon for efficient photocatalytic hydrogen evolution with synchronous highly selective oxidation of benzyl alcohol. *ACS Appl. Mater. Interfaces* **2022**, *14*, 13419−13430.

(21) Guo, F.; Hu, B.; Yang, C.; Zhang, J.; Hou, Y.; Wang, X. On-surface polymerization of in-plane highly ordered carbon nitride nanosheets toward photocatalytic mineralization of mercaptan gas. *Adv. Mater.* **2021**, *33*, 2101466.

(22) Zhai, B.; Li, H.; Gao, G.; Wang, Y.; Niu, P.; Wang, S.; Li, L. A crystalline carbon nitride based near-infrared active photocatalyst. *Adv. Funct. Mater.* **2022**, *32*, 2207375.

(23) Zhang, Q.; Chu, Y.-C.; Liu, Z.; Hong, M.; Fang, W.; Wu, X.-P.; Gong, X.-Q.; Chen, Z. Construction of triazine-heptazine-based carbon nitride heterojunctions boosts the selective photocatalytic C-C bond cleavage of lignin models. *Appl. Catal., B* **2023**, *331*, 122688.

(24) Zhang, G.; Xu, Y.; Liu, G.; Li, Y.; He, C.; Ren, X.; Zhang, P.; Mi, H. Pyrimidine donor induced built-in electric field between melon chains in crystalline carbon nitride to facilitate excitons dissociation. *Chin. Chem. Lett.* **2023**, *34*, 107383.

(25) Wang, W.; Shu, Z.; Liao, Z.; Zhou, J.; Meng, D.; Li, T.; Zhao, Z.; Xu, L. Sustainable one-step synthesis of nanostructured potassium poly(heptazine imide) for highly boosted photocatalytic hydrogen evolution. *Chem. Eng. J.* **2021**, *424*, 130332.

(26) Yu, S.; Zhao, P.; Yang, X.; Li, Q.; Mohamed, B. A.; Saad, J. M.; Zhang, Y.; Zhou, H. Low-temperature hydrothermal carbonization of pectin enabled by high pressure. *J. Anal. Appl. Pyrol.* **2022**, *166*, 105627.
(27) Chen, G.; Zhou, M.; Catanach, J.; Liaw, T.; Fei, L.; Deng, S.; Luo, H. Solvothermal route based in situ carbonization to Fe_3O_4@C as anode material for lithium ion battery. *Nano Energy* **2014**, *8*, 126−132.
(28) Zhang, W.; Peng, J.; Hua, W.; Liu, Y.; Wang, J.; Liang, Y.; Lai, W.; Jiang, Y.; Huang, Y.; Zhang, W.; Yang, H.; Yang, Y.; Li, L.; Liu, Z.; Wang, L.; Chou, S.-L. Architecting amorphous vanadium oxide/MXene nanohybrid via tunable anodic oxidation for high-performance sodium-ion batteries. *Adv. Energy Mater.* **2021**, *11*, 2100757.
(29) Li, C. C.; Wang, B.; Chen, D.; Gan, L.-Y.; Feng, Y.; Zhang, Y.; Yang, Y.; Geng, H.; Rui, X.; Yu, Y. Topotactic transformation synthesis of 2D ultrathin GeS_2 nanosheets toward high-rate and high-energy-density sodium-ion half/full batteries. *ACS Nano* **2020**, *14*, 531−540.
(30) Zhao, R.; Qian, Z.; Liu, Z.; Zhao, D.; Hui, X.; Jiang, G.; Wang, C.; Yin, L. Molecular-level heterostructures assembled from layered black phosphorene and Ti_3C_2 MXene as superior anodes for high-performance sodium ion batteries. *Nano Energy* **2019**, *65*, 104037.
(31) Tang, J.-Y.; Kong, X. Y.; Ng, B.-J.; Chew, Y.-H.; Mohamed, A. R.; Chai, S.-P. Midgap-state-mediated two-step photoexcitation in nitrogen defect-modified g-C_3N_4 atomic layers for superior photocatalytic CO_2 reduction. *Catal. Sci. Technol.* **2019**, *9*, 2335−2343.
(32) Kang, H.-J.; Lee, T.-G.; Kim, H.; Park, J.-W.; Hwang, H. J.; Hwang, H.; Jang, K.-S.; Kim, H. J.; Huh, Y. S.; Im, W. B.; Jun, Y.-S. Thick free-standing electrode based on carbon-carbon nitride microspheres with large mesopores for high-energy-density lithium-sulfur batteries. *Carbon Energy* **2021**, *3*, 410−423.
(33) Shen, Q.; Jiang, P.; He, H.; Feng, Y.; Cai, Y.; Lei, D.; Cai, M.; Zhang, M. Designing C_3N_4/N-rich carbon fiber composites for high-performance potassium-ion hybrid capacitors. *Energy Environ. Mater.* **2021**, *4*, 638−645.
(34) Weng, G.-M.; Xie, Y.; Wang, H.; Karpovich, C.; Lipton, J.; Zhu, J.; Kong, J.; Pfefferle, L. D.; Taylor, A. D. A promising carbon/g-C_3N_4 composite negative electrode for a long-life sodium-ion battery. *Angew. Chem., Int. Ed.* **2019**, *58*, 13727−13733.
(35) Ren, W.; Cheng, J.; Ou, H.; Huang, C.; Anpo, M.; Wang, X. Optimizing the crystallization process of conjugated polymer photocatalysts to promote electron transfer and molecular oxygen activation. *J. Catal.* **2020**, *389*, 636−645.
(36) Ren, W.; Cheng, J.; Ou, H.; Huang, C.; Titirici, M.-M.; Wang, X. Enhancing visible-light hydrogen evolution performance of crystalline carbon nitride by defect engineering. *ChemSusChem* **2019**, *12*, 3257−3262.
(37) Wang, W.; Fan, X.; Shu, Z.; Zhou, J.; Meng, D. Sustainable and mild exfoliation of bulk crystalline carbon nitride into ultrathin nanosheets via ion-exchange in pure-water. *Carbon* **2023**, *205*, 76−85.
(38) Yang, M.; Lian, R.; Zhang, X.; Wang, C.; Cheng, J.; Wang, X. Photocatalytic cyclization of nitrogen-centered radicals with carbon nitride through promoting substrate/catalyst interaction. *Nat. Commun.* **2022**, *13*, 4900.
(39) Xu, Y.; Fan, M.; Yang, W.; Xiao, Y.; Zeng, L.; Wu, X.; Xu, Q.; Su, C.; He, Q. Homogeneous carbon/potassium-incorporation strategy for synthesizing red polymeric carbon nitride capable of near-infrared photocatalytic H_2 production. *Adv. Mater.* **2021**, *33*, 2101455.
(40) Zhang, D.; Guo, Y.; Zhao, Z. Porous defect-modified graphitic carbon nitride via a facile one-step approach with significantly enhanced photocatalytic hydrogen evolution under visible light irradiation. *Appl. Catal., B* **2018**, *226*, 1−9.
(41) Pan, Y.; Chen, X.; Yin, S.; Zhou, F.; Hou, J.; Lu, L.; Ji, S.; Linkov, V.; Wang, P. Polysulfides immobilization and conversion by nitrogen-doped porous carbon/graphitized carbon nitride heterojunction for high-rate lithium-sulfur batteries. *Electrochim. Acta* **2022**, *423*, 140387.
(42) Xu, Y.; He, X.; Zhong, H.; Singh, D. J.; Zhang, L.; Wang, R. Solid salt confinement effect: An effective strategy to fabricate high crystalline polymer carbon nitride for enhanced photocatalytic hydrogen evolution. *Appl. Catal., B* **2019**, *246*, 349−355.
(43) Qian, Y.; Lai, H.; Ma, J.; Deng, G.; Long, B.; Song, T.; Liu, L.; Wang, X.; Tong, Y. Molten salt synthesis of KCl-preintercalated C_3N_4 nanosheets with abundant pyridinic-N as a superior anode with 10 K cycles in lithium ion battery. *J. Colloid Interface Sci.* **2022**, *606*, 537−543.
(44) Li, J.; Zhang, K.; Zhao, Y.; Wang, C.; Wang, L.; Wang, L.; Liao, M.; Ye, L.; Zhang, Y.; Gao, Y.; Wang, B.; Peng, H. High-efficiency and stable Li-CO_2 battery enabled by carbon nanotube/carbon nitride heterostructured photocathode. *Angew. Chem., Int. Ed.* **2022**, *61*, e202114612.
(45) Zheng, Y.; Luo, Y.; Ruan, Q.; Wang, S.; Yu, J.; Guo, X.; Zhang, W.; Xie, H.; Zhang, Z.; Huang, Y. Plasma-induced hierarchical amorphous carbon nitride nanostructure with two N_2 c-site vacancies for photocatalytic H_2O_2 production. *Appl. Catal., B* **2022**, *311*, 121372.
(46) Zhou, Y.; Zhang, S.; Xu, J.; Zhang, Y. Construction of MoS_2-nitrogen-deficient graphitic carbon nitride anode toward high performance sodium-ions batteries. *Mater. Lett.* **2020**, *273*, 127890.
(47) Chen, J.; Mao, Z.; Zhang, L.; Wang, D.; Xu, R.; Bie, L.; Fahlman, B. D. Nitrogen-deficient graphitic carbon nitride with enhanced performance for lithium ion battery anodes. *ACS Nano* **2017**, *11*, 12650−12657.
(48) Son, E. J.; Lee, S. H.; Kuk, S. K.; Pesic, M.; Choi, D. S.; Ko, J. W.; Kim, K.; Hollmann, F.; Park, C. B. Carbon nanotube-graphitic carbon nitride hybrid films for flavoenzyme-catalyzed photoelectrochemical cells. *Adv. Funct. Mater.* **2018**, *28*, 1705232.
(49) Zhu, X.; Xia, F.; Liu, D.; Xiang, X.; Wu, J.; Lei, J.; Li, J.; Qu, D.; Liu, J. Crumpling carbon-pillared atomic-thin dichalcogenides and cnts into elastic balls as superior anodes for sodium/potassium-ion batteries. *Adv. Funct. Mater.* **2023**, *33*, 2207548.
(50) Sang, J.; Zhang, X.; Liu, K.; Cao, G.; Guo, R.; Zhang, S.; Wu, Z.; Zhang, Y.; Hou, R.; Shen, Y.; Shao, G. Effective coupling of amorphous selenium phosphide with high-conductivity graphene as resilient high-capacity anode for sodium-ion batteries. *Adv. Funct. Mater.* **2023**, *33*, 2211640.
(51) Pei, Z.; Meng, Q.; Wei, L.; Fan, J.; Chen, Y.; Zhi, C. Toward efficient and high rate sodium-ion storage: A new insight from dopant-defect interplay in textured carbon anode materials. *Energy Storage Mater.* **2020**, *28*, 55−63.
(52) Yao, X.; Ke, Y.; Ren, W.; Wang, X.; Xiong, F.; Yang, W.; Qin, M.; Li, Q.; Mai, L. Defect-rich soft carbon porous nanosheets for fast and high-capacity sodium-ion storage. *Adv. Energy Mater.* **2019**, *9*, 1803260.
(53) Tang, Y.; Wang, X.; Chen, J.; Wang, X.; Wang, D.; Mao, Z. PVP-assisted synthesis of g- C_3N_4-derived N-doped graphene with tunable interplanar spacing as high-performance lithium/sodium ions battery anodes. *Carbon* **2021**, *174*, 98−109.
(54) Cheng, C.; Mao, L.; Kang, X.; Dong, C.-L.; Huang, Y.-C.; Shen, S.; Shi, J.; Guo, L. A high-cyano groups-content amorphous-crystalline carbon nitride isotype heterojunction photocatalyst for high-quantum-yield H_2 production and enhanced CO_2 reduction. *Appl. Catal., B* **2023**, *331*, 122733.
(55) Li, Z.; Qin, H.; Tian, W.; Miao, L.; Cao, K.; Si, Y.; Li, H.; Wang, Q.; Jiao, L. 3D Sb-based composite framework with gradient sodiophilicity for ultrastable sodium metal anodes. *Adv. Funct. Mater.* **2023**, 2301554.
(56) Zhang, X.; Weng, W.; Gu, H.; Hong, Z.; Xiao, W.; Wang, F.; Li, W.; Gu, D. Versatile preparation of mesoporous single-layered transition-metal sulfide/carbon composites for enhanced sodium storage. *Adv. Mater.* **2022**, *34*, 2104427.
(57) Yun, Y.; Xi, B.; Tian, F.; Chen, W.; Sun, W.; Pan, H.; Feng, J.; Qian, Y.; Xiong, S. Zero-strain structure for efficient potassium storage: Nitrogen-enriched carbon dual-confinement CoP composite. *Adv. Energy Mater.* **2022**, *12*, 2103341.

https://doi.org/10.1021/acsnano.3c10779
ACS Nano XXXX, XXX, XXX−XXX

(58) Li, Y.; Chen, M.; Liu, B.; Zhang, Y.; Liang, X.; Xia, X. Heteroatom doping: An effective way to boost sodium ion storage. *Adv. Energy Mater.* **2020**, *10*, 2000927.
(59) Adekoya, D.; Gu, X.; Rudge, M.; Wen, W.; Lai, C.; Hankel, M.; Zhang, S. Carbon nitride nanofibres with exceptional lithium storage capacity: From theoretical prediction to experimental implementation. *Adv. Funct. Mater.* **2018**, *28*, 1803972.
(60) Zhang, G.; Liu, M.; Heil, T.; Zafeiratos, S.; Savateev, A.; Antonietti, M.; Wang, X. Electron deficient monomers that optimize nucleation and enhance the photocatalytic redox activity of carbon nitrides. *Angew. Chem., Int. Ed.* **2019**, *58*, 14950−14954.
(61) Jiang, Y.; Wu, F.; Ye, Z.; Li, C.; Zhang, Y.; Li, L.; Xie, M.; Chen, R. Fe_2VO_4 nanoparticles anchored on ordered mesoporous carbon with pseudocapacitive behaviors for efficient sodium storage. *Adv. Funct. Mater.* **2021**, *31*, 2009756.
(62) Li, X.; Han, Z.; Yang, W.; Li, Q.; Li, H.; Xu, J.; Li, H.; Liu, B.; Zhao, H.; Li, S.; Wang, X.; Wu, X.-L. 3D ordered porous hybrid of ZnSe/N-doped carbon with anomalously high Na^+ mobility and ultrathin solid electrolyte interphase for sodium-ion batteries. *Adv. Funct. Mater.* **2021**, *31*, 2106194.
(63) Meng, W.; Dang, Z.; Li, D.; Jiang, L. Long-cycle life sodium-ion battery fabrication via unique chemical bonding interface mechanism. *Adv. Mater.* **2023**, *35*, 2301376.
(64) Chen, L.; Song, K.; Shi, J.; Zhang, J.; Mi, L.; Chen, W.; Liu, C.; Shen, C. PAANa-induced ductile SEI of bare micro-sized FeS enables high sodium-ion storage performance. *Sci. China Mater.* **2021**, *64*, 105−114.
(65) Chayambuka, K.; Mulder, G.; Danilov, D. L.; Notten, P. H. L. Sodium-ion battery materials and electrochemical properties reviewed. *Adv. Energy Mater.* **2018**, *8*, 1800079.
(66) Zhao, L.-F.; Hu, Z.; Lai, W.-H.; Tao, Y.; Peng, J.; Miao, Z.-C.; Wang, Y.-X.; Chou, S.-L.; Liu, H.-K.; Dou, S.-X. Hard carbon anodes: Fundamental understanding and commercial perspectives for Na-ion batteries beyond Li-ion and K-ion counterparts. *Adv. Energy Mater.* **2021**, *11*, 2002704.
(67) Liang, X.; Xue, S.; Yang, C.; Ye, X.; Wang, Y.; Chen, Q.; Lin, W.; Hou, Y.; Zhang, G.; Shalom, M.; Yu, Z.; Wang, X. The directional crystallization process of poly (triazine imide) single crystals in molten salts. *Angew. Chem., Int. Ed.* **2023**, *62*, e202216434.
(68) Li, R.; Wang, Y.; Xu, L.-C.; Shen, J.; Zhao, W.; Yang, Z.; Liu, R.; Shao, J.-L.; Guo, C.; Li, X. A boron-exposed TiB_3 monolayer with a lower electrostatic-potential surface as a higher-performance anode material for Li-ion and Na-ion batteries. *Phys. Chem. Chem. Phys.* **2020**, *22*, 22236−22243.
(69) Li, Y.; Han, M.; Zhou, Z.; Xia, X.; Chen, Q.; Chen, M. Topological insulator-assisted $MoSe_2/Bi_2Se$ heterostructure: Achieving fast reaction kinetics toward high rate sodium-ion batteries. *ChemElectroChem.* **2021**, *8*, 697−704.
(70) Chen, D.; Lu, R.; Yu, R.; Dai, Y.; Zhao, H.; Wu, D.; Wang, P.; Zhu, J.; Pu, Z.; Chen, L.; Yu, J.; Mu, S. Work-function-induced interfacial built-in electric fields in Os-$OsSe_2$ heterostructures for active acidic and alkaline hydrogen evolution. *Angew. Chem., Int. Ed.* **2022**, *61*, e202208642.
(71) Yu, Y.-X. Prediction of mobility, enhanced storage capacity, and volume change during sodiation on interlayer-expanded functionalized Ti_3C_2 mxene anode materials for sodium-ion batteries. *J. Phys.Chem. C* **2016**, *120*, 5288−5296.

https://doi.org/10.1021/acsnano.3c10779
ACS Nano XXXX, XXX, XXX−XXX